

Some First Steps Towards a Radiation GRMHD Code: Radiative Effects on Accretion Rate onto a Kerr Black Hole

Jean-Pierre De Villiers
Calgary, Alberta
email: jpd.asph@mac.com

February 8, 2008

Abstract

The role of radiation in general relativistic magnetohydrodynamic (GRMHD) accretion simulations is discussed through axisymmetric simulations of the evolution of an initial torus seeded with a weak magnetic field. The paper compares and contrasts the rate of accretion onto a Kerr black hole and mass flux out of the initial torus at large radii in the GRMHD code of De Villiers & Hawley and a newly developed radiative GRMHD code. This rGRMHD code currently operates in the diffusion approximation, restricting the study of radiative effects to the bound portion of the accretion disk/jet system. However, these preliminary findings suggest that radiative effects do play a potentially significant role in regulating the accretion flow.

1 Overview

The task of simulating accretion disks in black hole systems has seen much progress in recent years with the advent of general relativistic MHD (GRMHD) codes capable of simulating disks under not only under axisymmetry (Gammie, McKinney, & Toth, 2003) but also in three spatial dimensions (De Villiers & Hawley, 2003, hereafter DH03; and Mizuno *et al.*, 2006). In addition, the extraction of observables from such simulations has been described in the literature, with ray tracing techniques applied in a post-processing phase to numerical data generated by the GRMHD solver by Schnittman, Krolik, & Hawley (2006). However, it is understood that radiative processes can play a potentially significant role in the dynamics of black hole/disk/jet systems (Frank, King, & Raine, 2003). So, ideally, the task of simulating such systems should be undertaken with codes that capture not only the relativistic dynamics of the accreting gas and magnetic fields, but also treat the radiation field in a self-consistent manner. Results of non-relativistic radiative shearing box simulations have been reported by Hirose, Krolik, & Stone (2006), showing that radiative effects are important contributors to the dynamics of accretion flows. However, fully relativistic treatments of the radiation problem remain a rarity, even though discussion of the formalism can be

found in literature spanning several decades, from Lindquist (1966), through the standard reference by Mihalas & Weibel-Mihalas (1984; hereafter MM84), and recently in Takahashi (2007; hereafter T07), where a derivation of the equations of radiative hydrodynamics for the Kerr metric are given.

The objective of the project introduced here is to create a radiative GRMHD code to explore the effects of radiation on accretion disk simulations. The starting point is the GRMHD code of DH03, an explicit, finite difference solver that evolves the equations of general relativistic magnetohydrodynamics in the Kerr metric. Over a period of a few years the GRMHD code has been augmented by the addition of a ray tracing module which forms part of the code’s history mechanism. This module can produce fully ray-traced, time-ordered 2D pixel maps of emission processes captured as the simulation evolves; since the GRMHD code is a parallel MPI code, this extra component has been delegated to a slave processor so that the overall parallel efficiency of the original solver has not significantly degraded (though execution times are slower). More recently, a radiation component has been added to the code’s main physics loop, introducing the calculation of radiative effects to the source and transport steps that evolve the equations of energy and momentum conservation. Although these additions have greatly increased the complexity of the code, the ever-increasing power of desktop computing systems allows axisymmetric simulations to be readily carried out, and even modest 3D simulations are within the reach of such systems (though with turnaround times measured in weeks, if not months). Large-scale simulations with this new rGRMHD code remain in the realm of massively parallel high-performance computing systems, and lie beyond the scope of the project described here.

The addition of radiation to the energy/momentum equations represents only one of two major modifications to the rGRMHD code. The second is the introduction of the radiative transfer equation (RTE) to correctly capture the flow of radiation through the simulation volume; the addition of the RTE is an ongoing project. Since the modification of the dynamical equations is itself a significant change, it is desirable to test the code as it stands prior to investing further development time on the RTE. As it turns out, it is possible to decouple the dynamical equations from the RTE by working in the diffusion approximation, where the radiating fluid is assumed to be sufficiently opaque that the radiation field is thermal (MM84). The main computational advantage of the diffusion approximation is that the radiative effects can be obtained from fluid variables given the availability of a suitable opacity model. This approximation does, however, impose a set of restrictions since only certain portions of the simulation volume will satisfy its underlying conditions. The simulations described here study radiative effects in the bound portion of the accretion flow only, where the fluid is sufficiently dense. Radiative effects are switched off in the unbound regions, namely in the evacuated funnel where fast outflows and jets have been reported by De Villiers, Hawley, & Krolik (2003; hereafter DHK03). Since radiative effects in the dynamics of the outflows and jets are thought to be significant, the results of the simulations described here should be treated as informative, but certainly not definitive or comprehensive.

To perform this preliminary assessment of the importance of radiative effects on accretion, two families of axisymmetric simulations loosely based on model KDP of DHK03 are used to compare mass fluxes for different temperatures in the initial tori and two equations of state. In an effort to prevent the technical details from distracting from the results, a description of the present state of the rGRMHD code has been relegated to the appendices, and the emphasis of the body of the paper is on the simulations.

2 Initial State and Boundary Conditions

The earlier accretion studies of DHK03 and follow-on papers (Hirose *et al.*, 2004; De Villiers *et al.*, 2005; Krolik, Hawley, & Hirose, 2005) operated under the test fluid approximation, meaning that the mass-energy of the initial torus was effectively decoupled from the mass of the central black hole, so that simulations could equally be interpreted for accretion flows in systems of stellar or galactic-core scale. In incorporating radiative effects, this arbitrary scaling is no longer possible and the density and temperature of the initial torus must be calibrated to ‘realistic’ astrophysical conditions.

In constructing an initial state for the rGRMHD code, it is necessary to discretize an initial torus on a grid that provides both good spatial resolution and rapid numerical execution. These two constraints lead to the choice of a compact initial torus that has its pressure maximum very close to the black hole (hence the use of quotation marks in the preceding paragraph). Since the rGRMHD code uses extremal light-crossing time to set the time step size (DH03), no additional constraints are imposed by the addition of radiation. Radiative simulations are slower than their non-radiative counterparts, but this is only due to added computational complexity and not to overly restrictive time step sizes. The equations of the initial state are derived in DHK03 and summarized in Appendix G.

The general simulation parameters are listed in Table 1. As in earlier work, the grid is chosen to have 192 radial and polar zones, and one azimuthal zone (i.e. a $2.5D$ simulation). To make contact with earlier KDP simulations, the spin of the black hole is taken to be $a/M = 0.9$. The black hole is taken to be an AGN-class black hole with a mass of $10^8 M_\odot$. Two broad classes of simulations were carried out, distinguished by the stiffness of the equation of state; the Rad1 group has a relativistic adiabatic index, $\Gamma = 4/3$, while the Rad2 group has $\Gamma = 5/3$, as was done in DHK03.

Table 1: Simulation Parameters.

Simulation	a/M_{bh}	M_{bh}	Γ	Grid ($n_r \times n_\theta$)	r_{in}/M_{bh}	r_{out}/M_{bh}	$\Delta\theta$
Rad1	0.900	$10^8 M_\odot$	4/3	192×192	1.51	60.0	0.001π
Rad2	0.900	$10^8 M_\odot$	5/3	192×192	1.51	60.0	0.001π

The key parameters for the initial tori are summarized in Table 2. The initial state in each simulation is taken to be a $100 M_\odot$ torus orbiting an AGN-like Kerr black hole. Each torus is initialized with a weak MRI (Magneto-Rotational Instability) seed field as measured by the grid-averaged plasma β of 100. Each torus has an inner edge, r_{in} , at $6.80 M_{bh}$ (roughly $3 r_{ms}$, where $r_{ms} = 2.32 M_{bh}$ is the marginally stable orbit of a Kerr black hole with spin $a/M_{bh} = 0.9$). The pressure maximum in each simulation is at $12 M_{bh}$, corresponding to an orbital period of $276 M_{bh}$, where M_{bh} is the mass of the central black hole. This choice of pressure maximum was made to hasten the growth of the MRI, and lies much closer to the black hole than in the analogous KDP simulation of DHK03. The density at the pressure maximum is on the order of $10^{-6} g cm^{-3}$. The peak temperature of the initial torus is taken to be either 200 K, 300 K, 400 K, or 1000 K. These initial tori are labelled somewhat arbitrarily cold (C), warm (W), hot (H), and very hot (V). The particular choice of temperatures was made to allow for the run of temperatures in the accretion flow to lie in the range of $1000 \lesssim T_{acc} \lesssim 10,000$ K, which corresponds with the temperature range

of the zero-metallicity Rosseland mean opacity obtained by Lenzuni, Chernoff, & Salpeter (1991; hereafter LCS91). The typical densities in the initial tori also lie in the density range of this opacity function. For completeness, a reference simulation (labelled R) is also carried out with radiative effects switched off; this corresponds to simulations as would have been carried out with the original DH03 GRMHD code. Each simulation is allowed to evolve through the saturation phase of MRI, which occurs after a few orbits of the torus/disk at the initial pressure maximum; in axisymmetric simulations the MRI is not sustainable past a few orbits, so the simulations were terminated after five orbits at the pressure maximum.

Table 2: Initial Torus Parameters.

Model	Label	T_{disk}	M_{disk}	β	r_{in}/M_{bh}	r_{Pmax}/M_{bh}	T_{orb}/M_{bh}
Ref	R	200 K	$10^2 M_{\odot}$	100	6.80	12.0	276
Cold	C	200 K	$10^2 M_{\odot}$	100	6.80	12.0	276
Warm	W	300 K	$10^2 M_{\odot}$	100	6.80	12.0	276
Hot	H	400 K	$10^2 M_{\odot}$	100	6.80	12.0	276
Very Hot	V	1,000 K	$10^2 M_{\odot}$	100	6.80	12.0	276

For all simulations, the inner radial boundary is set at $1.51 M_{bh}$, the outer radial boundary is at $60 M_{bh}$, the polar boundaries are at $\pi \times 10^{-3}$ radians from the polar axes. Radial grid zones use exponential scaling; polar zones use a linear scaling; these have the effect of concentrating the computational zones near the event horizon. Outflow boundary conditions are in effect at the inner and outer radial boundaries (the outer boundary imposes an initial dust inflow until the outward accretion flow from the funnel/jet and the outward motion of the outer edge of the accretion disk are established). Reflecting boundary conditions are applied at the edges of the polar grid. Periodicity is applied on the azimuthal grid faces.

3 Results

The simulations discussed in this paper are used to address a narrowly focused question: what is the influence of radiation on mass flux in the accretion disk? Of particular interest is the effect of radiation in the hot, dense plunging flow near the black hole.

3.1 Overall Evolution

The set of ten simulations discussed here fall into two broad categories, sorted by adiabatic index (see Table 1). Within each category, one non-radiative and four radiative simulations were carried out. The four radiative simulations are distinguished by the initial temperature of the torus. As each simulation evolves, the overall characteristics described previously in DHK03 still apply (see, e.g., Figs. 2 and 3 of DHK03): the seed magnetic field in the initial torus is amplified by shearing; during the first orbit, a thin stream of accreting matter threads its way along the equatorial plane towards the black hole. The Magneto-Rotational Instability (MRI; Balbus & Hawley, 1998) peaks

during the second orbit of the main disk, driving a very active turbulent phase where angular momentum is transported outwards. With peak MRI activity, a good deal of matter is driven towards the black hole, and at the same time the outer edge of the initial torus begins an outward migration. In addition, a two-component outflow develops in the evacuated funnel, consisting of a relativistic, low density component along the axes of the black hole, and a denser, slower outflow along the funnel wall. Since the MRI is not sustainable in axisymmetry, turbulence subsides after a few orbits of the main disk. Peak activity occurs between two and three orbital periods at the initial pressure maximum.

As gas spirals on along the equatorial plane towards the black hole, it is compressed and heated, with temperature rising by an order of magnitude or so as the flow converges on the inner radial boundary. Since the radiation tensor in the diffusion approximation is set by the temperature and density of the gas, radiative effects “follow” the accretion flow and build up in the plunging region because of the elevated temperature there. However, radiative effects are also quite noticeable within the body of the disk as well, especially near the expanding outer edge where density drops and temperature rises.

3.2 Density Profile

The presence of radiation alters the distribution of gas within the disk. This can be seen in Figure 1, where plots of density are shown for two Rad1 simulations, reference simulation Rad1R and its hot counterpart Rad1H. The plots are time-averaged over the interval from $t = 2T_{\text{orb}}$ to $3T_{\text{orb}}$, corresponding to peak MRI activity. The plots are shown in coordinate space, which emphasizes the region inward of the pressure maximum, where the radial grid is concentrated.

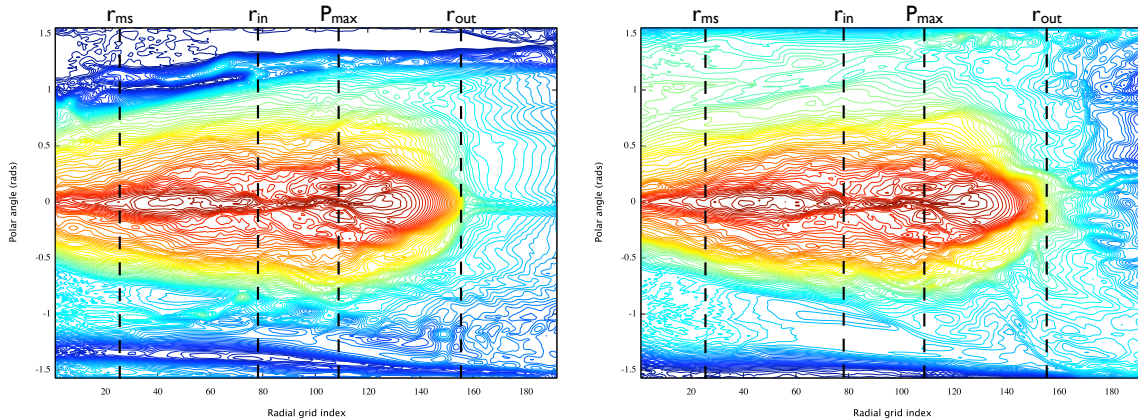


Figure 1: Density profiles, $\bar{\rho}(r, \theta)$, averaged over one orbit, comparing the reference run Rad1R (left panel) and the hot simulation Rad1H (right panel). The average is taken between $t = 2T_{\text{orb}}$ to $3T_{\text{orb}}$ as measured at the initial pressure maximum. Contours are logarithmic and are equally spaced over 10 decades, scaled to the initial maximum density. Plots are shown in coordinate space, with the polar angle referenced to the equatorial plane. For reference, vertical dashed lines indicate the location of the marginally stable orbit, as well as the inner edge, pressure maximum and outer edge of the initial torus.

Though the overall structure of the denser parts of the accretion disks is similar, as shown by the family of red contours, it is apparent that the funnel contains denser gas in Rad1H than it does in Rad1R, so even though radiative effects are switched off in the unbound funnel, differences due to radiation in the bound portion can influence the structure of the funnel (this underscores the importance of a proper radiative treatment in all regions of the simulation volume). In addition, there is a notable difference in the structure of the disk at large radii. It appears as if the radiative simulation shows a disk with a greater outward transport of material. Any differences in the structure of the plunging flow are hard to discern in these plots.

Similar outcomes, altered funnel density and greater outward migration of the disk at large radii, are seen in all radiative simulations.

3.3 Temperature Profile

The radial run of temperature covering the plunging flow and the main disk body is shown in Figure 2 for all simulations. Each curve represents averages of temperature in the vicinity of the equatorial plane. Steep rises in temperature are seen both in the direction of the black hole, and also in the bound, low density outer region of the disk (the outer edge of the initial torus lies at $r = 30 M_{bh}$). Since radiative effects in the diffusion approximation are directly tied to local temperature, it is to be expected that both the plunging flow and the outer edge of the disk should be locales where radiative effects might show the greatest divergence from the reference simulations. The reference simulations are plotted using the same temperature scaling as their cold counterparts (i.e. assuming a $200 K$ non-radiating initial torus).

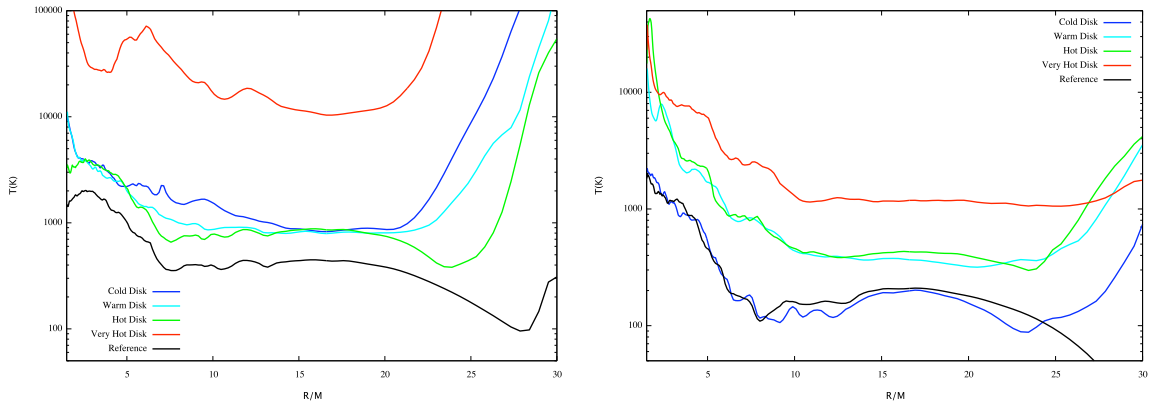


Figure 2: Run of temperature near equator for Rad1 (left panel) and Rad2 (right panel) simulations. The reference simulation in each family is plotted using the same temperature scaling factor as the corresponding cold simulation.

The temperature distribution in each simulation shows unique characteristics due to the interaction of the radiative terms with the other components of the GRMHD equations; the curves are not merely shifted vertically by the different temperature scalings used in each simulation. Though the temperature profile through the main disk body ($10 M_{bh} < r < 20 M_{bh}$) is relatively flat in all simulations, there is an order of magnitude rise from the inner edge of the disk to the inner radial

boundary in the Rad1 simulations, and a steeper rise in the Rad 2 simulations. There is also a steep rise in temperature from $r \approx 25 M_{bh}$ outward; the rise is steeper in the Rad1 family than in the Rad2 family. In both families of simulations, this upturn in temperature at large radii is unique to the radiative simulations, and is absent from the reference simulations. In the Rad2 family, the Rad2R and Rad2C temperature profiles closely parallel one another for $r < 25 M_{bh}$, while in the Rad1 family, the Rad1R and Rad1C profiles are quite distinct.

3.4 Accretion Rate

Perhaps the simplest diagnostic to quantify the role of radiation in the simulations is the shell-averaged radial transport of matter, $\dot{M} = \langle \rho U^r \rangle(r, t)$. This diagnostic, when plotted near the inner boundary, measures the rate of accretion onto the black hole as a function of time. Figure 3 shows the accretion rates for the Rad1 and Rad2 families. Though the graphs show a good deal of variability, it is nonetheless possible to see that notable departures from the reference simulations take place when radiative effects are added. The accretion rate is zero during the first orbit of

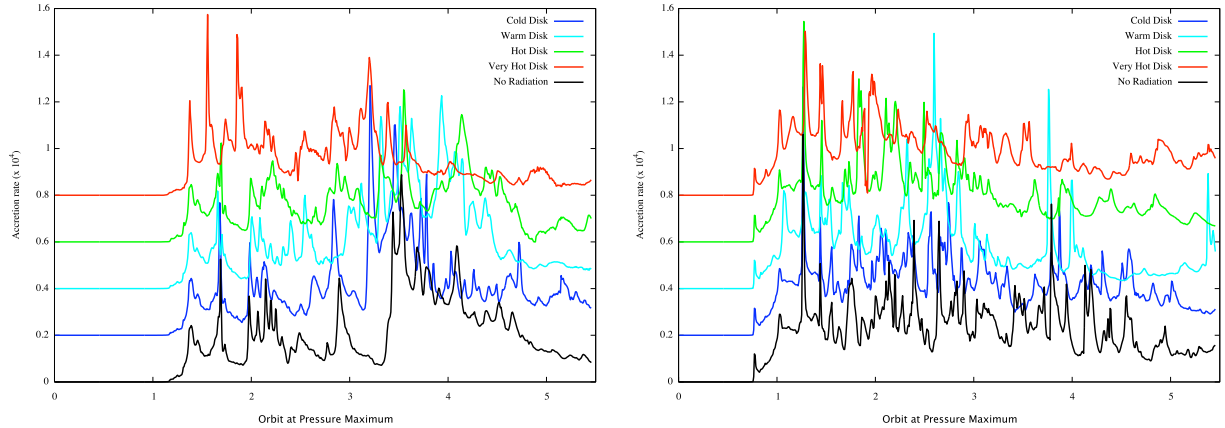


Figure 3: Accretion rate $\langle -\rho U^r \rangle(r_{inner}, t)$ through inner radial boundary for Rad1 (left panel) and Rad2 (right panel) simulations. Accretion rate is expressed as a fraction of the initial torus mass.

the Rad1 tori while the leading edge of the plunging flow makes it way towards the black hole. Material arrives slightly earlier for the Rad2 simulations. The rate of accretion is highly variable in all simulations, with several sharp peaks marking the arrival of dense knots of material from the accretion disk. In the early stages (between orbits 1 and 2), all accretion rate curves are essentially identical; as the plunging flow builds up and temperature rises, radiative effects begin to assert themselves. Beyond orbit 2, there are notable differences in the number, location, and amplitude of peaks in accretion rate between the simulations, though any trends are difficult to make out in these plots. In all cases, the rate of accretion decreases both in intensity and variability after four orbital periods due to a decrease in MRI-driven turbulence. The peak accretion rates, with values on the order of 10^{-4} , agree with the full 3D simulations of DHK03 as well as axisymmetric simulations of disks embedded in large-scale fields reported by De Villiers (2006).

A more quantitative measure is obtained by summing the $\langle -\rho U^r \rangle(r_{inner}, t)$ diagnostic over time

to obtain a measure of total accreted mass. These sums, normalized to the reference simulations Rad1R and Rad2R are given in Table 3. It is clear from the table that the cold simulations Rad1C

Table 3: Relative Accreted Mass, $M_{\text{rad}}/M_{\text{ref}}$.

Model/ Simulation	Rad1 ($\Gamma = 4/3$)	Rad2 ($\Gamma = 5/3$)
C	1.03	0.96
W	1.08	0.74
H	0.77	0.83
V	0.61	0.77

and Rad2C do not significantly differ in overall accretion from the reference simulations. However, important differences arise for the hotter initial tori, which build up higher temperatures in the plunging region. The Rad1 models ($\Gamma = 4/3$) seem to show a steady drop in accreted mass with higher initial temperature, while the Rad2 models ($\Gamma = 5/3$) show a reduced amount of accreted mass for the W, H, and V simulations, without an apparent trend.

As noted in §3.2, the density profiles suggest that a greater density is found at large radii in the radiative simulations than in the reference simulations. Also, as noted in §3.3, a steep rise in temperature is also seen in the outer portions of the disk, suggesting that radiation is acting to increase the temperature in this region. Are the two related? Figure 4 shows the mass flux diagnostic plotted at $r = 30 M_{\text{bh}}$; this tracks the passage of matter at a point just outside the outer edge of the initial torus for the Rad1 and Rad2 families of simulations. The departure from the reference simulation (black line) is remarkable. Even though there are large excursions in both directions, radiative effects in this region significantly enhance the net outward flow of matter from within the core of the accretion disk.

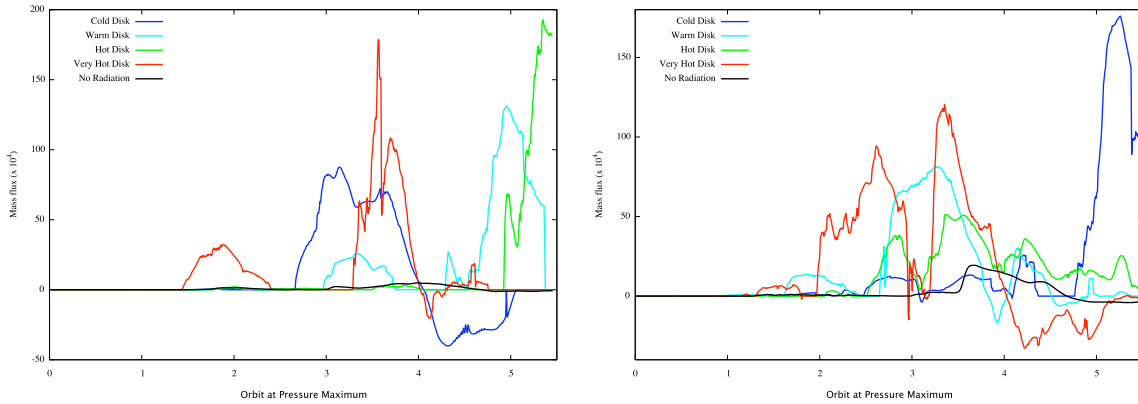


Figure 4: Mass flux $\langle \rho U^r \rangle(30 M_{\text{bh}}, t)$ past outer edge of initial torus for Rad1 (left panel) and Rad2 (right panel) simulations. Mass flux is expressed as a fraction of the initial torus mass.

3.5 Radiation Field

All components of the radiation tensor are dumped periodically, along with other code variables. Figure 5 shows the time-averaged structure of the radiative energy density (the time-time component of the radiation tensor, \mathbf{R}^{tt}), in the Boyer-Linquist frame for the Rad1H and Rad2H simulations; similar plots are obtained for the other simulations. The figure shows the effect of the switch controlling the radiative effects: the white patches at high and low polar angles are unbound regions where the radiation tensor is zeroed out. In both plots, the largest values of the radiative energy density straddle the plunging flow, in a region where the density is lower and temperature hotter than in the plunging flow. There is also a visible increase in intensity along the equator towards the black hole. Large streaks of bound material also occupy the funnel region in the two simulations; they represent the passage of clumps of bound, hot gas through the funnel (clumps of bound gas have turning points at large radii, but for these simulations, they exit the outer radial boundary).

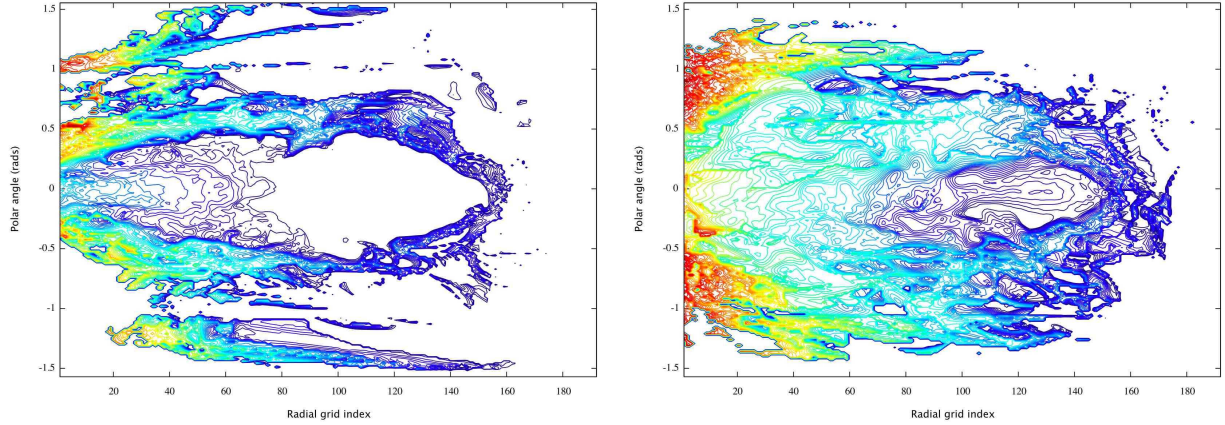


Figure 5: Plot of time-averaged $\mathbf{R}^{tt}(r, \theta)$ for the Rad1H (left panel) and Rad2H (right panel) simulations. The average is taken between $t = 2T_{\text{orb}}$ to $3T_{\text{orb}}$ as measured at the initial pressure maximum. Contours are logarithmic and are equally spaced over 13 decades. Plots are shown in coordinate space, with the polar angle referenced to the equatorial plane. Both plots use the same absolute log scaling.

It is apparent from this figure that the boundary between the bound and unbound portions of the simulation volume could give rise to very large gradients in the components of the radiation tensor, and could prove destabilizing. To guard against this, the portions of the code implementing radiative updates in the energy and momentum equations detect and prevent steep gradients due to zero values in the radiation tensor from entering the numerical solution. This limiter will be removed when the full version of the rGRMHD code is implemented.

4 Discussion and Conclusions

This brief paper has introduced a set of simulations meant to perform an initial validation of a new rGRMHD code that incorporates radiative effects into the dynamical equations, but does not yet implement the numerical solution of the Radiative Transfer Equation (RTE). By using the diffusion approximation, it is possible to prescribe the radiation tensor based on local properties of the fluid, without requiring a solution of the RTE. Even in this partial implementation, the rGRMHD code tracks properties of the radiation field (energy density, pressure, fluxes), and reports these through the history diagnostics and binary dumps. Quantitative analysis of in-situ effects of radiation is now possible, and with the ray tracing capabilities built into the code, detailed simulated observations are also within reach (though, as discussed in the appendices, such simulated observations are much more meaningful in full 3D simulations with sizable simulation volumes).

Though the numerical solutions produced a large amount of diagnostic information, this preliminary analysis focused on a very simple question: does the presence of radiation affect the transport of matter through the accretion disk?

Qualitatively, the simulations have shown that density and temperature in the accretion disk and plunging region are affected by the radiation field: details of the run of temperature in the plunging region and in the outer region of the disk depend on the initial strength of the radiation field (which is set by the model-dependent disk temperature); radiation is also found to enhance the outward transport of matter from the accretion disk. The cold initial tori tend to track the evolution of the reference simulations (which do not include radiative effects), suggesting the radiative results converge on the non-radiative results for weak radiation fields. The agreement between cold and reference simulations is best for the simulations using $\Gamma = 5/3$. Significant departures in density and temperature profiles are found for stronger initial radiation fields (i.e. hotter initial tori).

Quantitative analysis relied on a well-exercised diagnostic, radial mass flux $\langle \rho U^r \rangle(r, t)$, as a means of comparing radiative and non-radiative simulations. This diagnostic shows that the amount of matter accreted onto the black hole and the amount of matter transported outward from the main body of the disk are affected by radiation: accretion near the event horizon is reduced and matter transport at large radii is enhanced. For the simulations using a relativistic equation of state ($\Gamma = 4/3$) there seems to be a reduction in accretion that scales with temperature (hotter plunging flows tend to produce less accretion onto the black hole); for the adiabatic equation of state ($\Gamma = 5/3$), accretion is reduced by radiation from a hot inflowing gas, but the evidence for a clear temperature trend is not obvious. The accretion rates shown in Figure 3, when summed over the orbit where peak MRI activity occurs (between $t = 2 T_{\text{orb}}$ to $3 T_{\text{orb}}$ as measured at the initial pressure maximum), correspond to a rate on the order of one solar mass per year, a number that seems reasonable for relatively cold disks feeding AGN-scale systems.

It would be interesting at some later time to investigate whether accretion can be completely shut off by radiative effects in these types of simulations, and to investigate this outcome in relation to the general analyses of the Eddington limit (Frank, King, & Raine, 2003). This would most likely require the full rGRMHD code (with RTE), or at least the current code with an opacity function spanning a greater temperature range than LCS91. Ultimately, it is hoped that a proper treatment of the RTE will help shed light on the role of radiation not only in regulating accretion,

but also in powering the jets and funnel outflows; though these features have already been noted in the non-radiative DHK simulations, it remains important to clarify the role of radiation in these energetic processes. Figure 5 is especially suggestive in this regard: though the effects described here apply to the dense plunging flow, the radiation field is very intense in the region straddling this flow (and would likely be even greater at the base of the funnel if the current implementation did not switch off the radiation field there), so that the jets emerging from a fully radiative treatment would likely receive a substantial push from the intense radiation above the black hole pole caps.

The initial tori chosen for these simulations are very compact and produce prompt accretion. This was done by design to achieve a rapid turn-around time, and is justified because of the emphasis on accretion rate in the plunging flow. Drawing conclusions beyond this narrowly framed question seems inappropriate. Caution is also in order even in this limited interpretation of the simulations. The original GRMHD code has grown substantially in complexity, and a large number of diagnostics have been added, so that it will take time to develop a body of knowledge around this new data. For the time being, it seems wise to err on the side of caution when interpreting simulation outcomes by looking primarily for effects that reveal unambiguous trends across families of simulations when referenced to the existing base of knowledge from non-radiative GRMHD simulations.

As a final note, in recent years, a number of studies have relied on the accretion rate produced by non-radiative simulations as a proxy for dissipation, or have used the outcome of non-radiative simulations and applied ray tracing methods in a post-processing phase to approximate a radiating fluid. Figures 1, 2, and 3 show that radiation alters the detailed structure and time-dependence of the accretion flow from the non-radiative reference simulations. If nothing else, these simulations have demonstrated that reliance on post-processing of non-radiative simulations for emission studies is of limited use: radiation can substantially alter an accretion flow and must be treated in a self-consistent manner.

Acknowledgements:

Although the development of the full rGRMHD code is an independent research project, preliminary work on the ray tracing component was undertaken while the author was at the University of Virginia (2000-2004), supported by NSF grants AST-0070979 and PHY-0205155, and NASA grant NAG5-9266 (Principal Investigators John Hawley and Steve Balbus).

All simulations were carried out on an 8-core Mac Pro 3 GHz Xeon system with 2GB of RAM. Source code for this project was compiled with the GNU gfortran compiler and OpenMPI libraries. Graphics for this paper were generated using the GNU Octave application.

References

- [1] Balbus, S. A. & Hawley, J. F. 1998, *Rev. Mod. Phys.*, 70, 1
- [2] De Villiers, J. P. & Hawley, J. F. 2003, *ApJ*, 589, 458 (DH03)
- [3] De Villiers, J. P., Hawley, J. F., & Krolik, J. H. 2003, *ApJ*, 599, 1238 (DHK03)
- [4] De Villiers, J. P., Hawley, J. F., Krolik, J. H., & Hirose, S. 2005, *ApJ*, 620, 878

- [5] De Villiers, J. P. 2006, astro-ph/0605744
- [6] Frank, J., King, A., & Raine, D. 2002, *Accretion Power in Astrophysics*, 3rd ed. (Cambridge)
- [7] Hawley, J. F., Smarr, L. L., & Wilson, J. R., 1984, *ApJ*, 277, 296 (HSW)
- [8] Hirose, S., Krolik, J. H., De Villiers, J. P., & Hawley, J. F. 2004, *ApJ*, 606, 1083
- [9] Hirose, S., Krolik, J. H., & Stone, J. M. 2006, *ApJ*, 640, 901
- [10] Krolik, J. H., Hirose, S., & Hawley, J. F. 2005, *ApJ*, 620, 878
- [11] Lenzuni, P., Chernoff, D. F., & Salpeter, E. E. 1991, *ApJS*, 76, 758 (LCS91)
- [12] Lindquist, R. W. 1966, *Annals of Physics*, 37, 487
- [13] Gammie, C. F., McKinney, J. C., & Toth, G. 2003, *ApJ*, 589, 444
- [14] Mihalas, D., & Weibel-Mihalas, B. 1984. *Foundations of Radiation Hydrodynamics* (Mineola:Dover).
- [15] Misner, C. W., Thorne, K. S., & Wheeler, J. A, 1973, *Gravitation* (San Francisco: W.H. Freeman)
- [16] Mizuno, Y., Nishikawa, K.-I., Koide, S., Hardee, P., & Fishman, G. J., 2006, <http://arxiv.org/abs/astro-ph/0609004v1>
- [17] Press, W. H., Flannery, B. P., Teukolsky, S. A., & Vetterling, W. T. 1992, *Numerical Recipes in FORTRAN 77: The Art of Scientific Computing* (Cambridge)
- [18] Reynolds, C. S., Young, A. I., Begelman, M. C., & Fabian, A. C., 1998 *ApJ*, 514, 164
- [19] Schnittman, J. D., Krolik, J. H., & Hawley, J. F. 2006, *ApJ*, 651, 1031
- [20] Takahashi, R., 2007, *MNRAS*, 382, 1041 (T07)

Appendices - Building The rGRMHD Code

Introducing a radiation mechanism to the GRMHD code is not a trivial undertaking and the process has been broken down into a series of steps, each outlined in the following appendices. This paper builds upon the discussion in DH03 and DHK03, and the reader unfamiliar with the original GRMHD code should refer to these papers prior to reading the following descriptions. A general derivation of the equations of radiative hydrodynamics in the Kerr metric can be found in T07, and complements the numerically oriented treatment discussed here in the MHD context.

A Equations of Radiative GRMHD

In the GRMHD code of DH03, the state of the relativistic test fluid at each point in the spacetime is described by its density, ρ , internal energy, ϵ , 4-velocity U^μ , and isotropic pressure, P , which is related to the first two scalars via the equation of state of an ideal gas, $P = \rho \epsilon (\gamma - 1)$, where γ is the adiabatic exponent. The relativistic enthalpy is $h = 1 + \epsilon + P/\rho$. This set of variables needs to be augmented to include the presence of a radiation field.

The rGRMHD code continues to use the Boyer-Lindquist coordinate system as the main reference frame for the simulations. However, radiative effects are best calculated in the frame of reference that is locally comoving with the radiating fluid (MM84), necessitating the introduction of coordinate transformations that will be discussed in greater detail in Appendix B. In the following description, all vector and tensor quantities are expressed in the Boyer-Lindquist reference frame. The Boyer-Lindquist frame constitutes a coordinate basis, for which the following identities for the divergence of a four-vector and a tensor can be used to simplify expressions:

$$\nabla_\mu (f v^\mu) = \frac{1}{\sqrt{-g}} \partial_\mu (\sqrt{-g} f v^\mu), \quad (1)$$

$$\nabla_\mu (\beta^{\mu\nu}) = \frac{1}{\sqrt{-g}} \partial_\mu (\sqrt{-g} \beta^{\mu\nu}) + \Gamma_{\epsilon\mu}^\nu \beta^{\mu\epsilon}. \quad (2)$$

Greek indices range over all four spacetime coordinates, while roman indices range over spatial coordinates only.

The equations of ideal GRMHD are the law of baryon conservation,

$$\nabla_\mu (\rho U^\mu) = 0, \quad (3)$$

where ∇_μ is the covariant derivative, the conservation of stress-energy,

$$\nabla_\mu T^{\mu\nu} = 0, \quad (4)$$

where $T^{\mu\nu}$ is the energy-momentum tensor for the fluid, and the induction equation,

$$\partial_j (\mathcal{B}^j) = 0 \quad (\nu = 0), \quad (5)$$

$$\partial_t (\mathcal{B}^i) - \partial_j (V^i \mathcal{B}^j - \mathcal{B}^i V^j) = 0 \quad (\nu = i), \quad (6)$$

where \mathcal{B}^i are the components of the Constrained-Transport magnetic field, and the transport velocity (also known as the coordinate velocity) V^μ is defined $V^\mu = U^\mu/U^t$, where $U^t = W/\alpha$, and W is

the relativistic gamma-factor. The magnetic field is also described by the magnetic field 4-vector, b^μ . The latter is fundamental to the definition of the total four momentum,

$$S_\mu = (\rho h + \|b\|^2) W U_\mu, \quad (7)$$

and the normalization condition

$$g^{\mu\nu} S_\mu S_\nu = -\left[(\rho h + \|b\|^2) W\right]^2, \quad (8)$$

which is algebraically equivalent to the usual normalization condition $U^\mu U_\mu = -1$. We define auxiliary density and energy functions $D = \rho W$ and $E = D \epsilon$. The set of variables D , E , S_μ , \mathcal{B}^i , V^i , and b_μ constitute the fundamental GRMHD code variables.

The equations of GRMHD are augmented by the contribution from a radiation field in a straightforward manner, by adding a radiative contribution to the energy-momentum tensor,

$$\mathbf{T}^{\mu\nu} = \mathbf{T}_{(\text{fluid})}^{\mu\nu} + \mathbf{T}_{(\text{EM})}^{\mu\nu} + \mathbf{R}^{\mu\nu} \quad (9)$$

where

$$\mathbf{T}_{(\text{fluid})}^{\mu\nu} = \rho h U^\mu U^\nu + P g^{\mu\nu} \quad (10)$$

$$\mathbf{T}_{(\text{EM})}^{\mu\nu} = \left(\frac{1}{2} g^{\mu\nu} \|b\|^2 + U^\mu U^\nu \|b\|^2 - b^\mu b^\nu \right) \quad (11)$$

$$\mathbf{R}^{\mu\nu} = \left[\begin{array}{c|c} \mathcal{E} & \mathcal{F}^j \\ \hline \mathcal{F}^i & \mathcal{P}^{ij} \end{array} \right] \quad (12)$$

where the radiation tensor, $\mathbf{R}^{\mu\nu}$, contains \mathcal{E} is the radiative energy density, \mathcal{F} the radiative flux, and \mathcal{P} the radiative stress; respectively the zeroth, first, and second moments of the radiation field. These components are evaluated using

$$\mathbf{R}^{\mu\nu} = \int \oint \mathcal{I}(\mathbf{n}, \nu) n^\mu n^\nu d\Omega d\nu \quad (13)$$

where \mathcal{I} is the intensity of the radiation field, \mathbf{n} is the direction 4-vector. In a complete treatment of radiation, the intensity is given by the radiative transfer equation (RTE). In the current implementation, evaluation of the radiation tensor is greatly simplified by using the first-order diffusion approximation, which directly prescribes $\mathbf{R}^{\mu\nu}$ from the temperature and mean opacity of the gas (see Appendix C). Inclusion of the RTE is the subject of ongoing work and is not described here.

Radiative contributions enter the GRMHD code through the energy and momentum equations, and the derivation proceeds as described in DH03. The equation of energy conservation is obtained by projecting the conservation law $\nabla_\mu \mathbf{T}^{\mu\nu} = 0$ onto the fluid 4-velocity:

$$U_\nu \nabla_\mu \mathbf{T}^{\mu\nu} = 0, \quad (14)$$

which expands to

$$U_\nu \nabla_\mu \mathbf{T}^{\mu\nu} = U_\nu \nabla_\mu \left\{ \left(\rho h + \|b\|^2 \right) U^\mu U^\nu + \left(P + \frac{\|b\|^2}{2} \right) g^{\mu\nu} - b^\mu b^\nu + \mathbf{R}^{\mu\nu} \right\} = 0. \quad (15)$$

By using the law of baryon conservation (3), we recover after some algebra the local energy conservation law which now includes the projection of the divergence of the radiation tensor:

$$\nabla_\mu (\rho \epsilon U^\mu) + P \nabla_\mu U^\mu - U^\nu \nabla_\mu \mathbf{R}^\mu{}_\nu = 0. \quad (16)$$

Applying the definition for the auxiliary energy function E , and also using

$$\Gamma_{\mu\nu}{}^\gamma \mathbf{\Pi}_\gamma{}^\mu = \frac{1}{2} \mathbf{\Pi}^{\gamma\mu} \partial_\nu g_{\mu\gamma} = -\frac{1}{2} \mathbf{\Pi}_{\gamma\mu} \partial_\nu g^{\mu\gamma} \quad (17)$$

in expanding the radiation term, the energy equation is rewritten as follows:

$$\begin{aligned} \partial_t (E) + \frac{1}{\sqrt{\gamma}} \partial_i (\sqrt{\gamma} E V^i) + P \partial_t (W) + \frac{P}{\sqrt{\gamma}} \partial_i (\sqrt{\gamma} W V^i) - \frac{W}{\alpha} \partial_t \mathbf{R}^t{}_t - \\ \frac{W}{\alpha} V^i \partial_t \mathbf{R}^t{}_i - \frac{W}{\alpha^2 \sqrt{\gamma}} \partial_j (\alpha \sqrt{\gamma} \mathbf{R}^j{}_t) - \frac{W}{\alpha^2 \sqrt{\gamma}} V^i \partial_j (\alpha \sqrt{\gamma} \mathbf{R}^j{}_i) - \frac{1}{2} \mathbf{R}_{\mu\epsilon} \frac{W}{\alpha} V^k \partial_k g^{\mu\epsilon} = 0, \end{aligned} \quad (18)$$

where the contributions from the various moments of the radiation field significantly alter the structure of the equation, introducing additional transport terms and, new to this portion of the code, metric derivatives. The components of the radiation tensor, $\mathbf{R}^\mu{}_\nu$ and $\mathbf{R}_{\mu\nu}$, have been left in their unsimplified form and are obtained from $\mathbf{R}^{\mu\nu}$ prescribed by the diffusion approximation by lowering indices with the metric tensor.

The momentum conservation equations follow from applying the projection tensor $h_{\mu\nu} = g_{\mu\nu} + U_\mu U_\nu$ to conservation law (4), leading to $\nabla_\mu \mathbf{T}^\mu{}_\nu = 0$. Expanding,

$$\nabla_\mu \mathbf{T}^\mu{}_\nu = \nabla_\mu \left\{ \left(\rho h + \|b\|^2 \right) U^\mu U_\nu + \left(P + \frac{\|b\|^2}{2} \right) \delta^\mu{}_\nu - b^\mu b_\nu + \mathbf{R}^\mu{}_\nu \right\} = 0. \quad (19)$$

Using the definition of momentum S_ν the first term in the preceding expression can be rewritten as $S_\nu V^\mu / \alpha$ and simplified to $S_\nu S^\mu / \alpha S^t$, and applying (2) and (17) to the radiation component, we rewrite the momentum equation as

$$\begin{aligned} \frac{1}{\alpha \sqrt{\gamma}} \partial_\mu \sqrt{\gamma} S_\nu V^\mu + \frac{1}{2\alpha} \frac{S_\alpha S_\beta}{S^t} \partial_\nu g^{\alpha\beta} + \partial_\nu \left(P + \frac{\|b\|^2}{2} \right) - \frac{1}{\alpha \sqrt{\gamma}} \partial_\mu \alpha \sqrt{\gamma} b^\mu b_\nu - \\ \frac{1}{2} b_\alpha b_\beta \partial_\nu g^{\alpha\beta} + \partial_t \mathbf{R}^t{}_\nu + \frac{1}{\alpha \sqrt{\gamma}} \partial_i (\alpha \sqrt{\gamma} \mathbf{R}^i{}_\nu) + \frac{1}{2} \mathbf{R}^{\mu\epsilon} \partial_\nu (g_{\mu\epsilon}) = 0. \end{aligned} \quad (20)$$

To obtain the final form of the equations, multiply (20) by the lapse α , split the μ index into its space (i) and time (t) components, and restrict ν to the spatial indices (j) only:

$$\begin{aligned} \partial_t (S_j - \alpha b_j b^t + \alpha \partial_t \mathbf{R}^t{}_j) + \frac{1}{\sqrt{\gamma}} \partial_i \sqrt{\gamma} (S_j V^i - \alpha b_j b^i + \alpha \partial_t \mathbf{R}^i{}_j) + \\ \frac{1}{2} \left(\frac{S_\epsilon S_\mu}{S^t} - \alpha b_\mu b_\epsilon + \alpha \mathbf{R}_{\mu\epsilon} \right) \partial_j g^{\mu\epsilon} + \alpha \partial_j \left(P + \frac{\|b\|^2}{2} \right) = 0. \end{aligned} \quad (21)$$

B Constructing the Radiation Tensor

The radiation tensor is most easily computed in the reference frame that is locally comoving with the fluid (MM84). Since the rGRMHD code uses Boyer-Lindquist coordinates, it is necessary to introduce transformations that translate between the two reference frames. This is done in two stages, first by transforming the Boyer-Lindquist coordinate basis to its corresponding orthonormal basis (i.e. the ZAMO or LNRF frame; see Misner, Thorne & Wheeler, 1973), and then applying a Lorentz boost from this frame to the comoving frame.

In the Boyer-Lindquist frame, denote the radiation tensor with plain indices, $\mathbf{R}^{\mu\nu}$; in the orthonormal frame, denote it with carets, $\mathbf{R}^{\hat{\mu}\hat{\nu}}$; and in the comoving frame, denote it with tildes, $\mathbf{R}^{\tilde{\mu}\tilde{\nu}}$. The transformation from the Boyer-Lindquist frame to the orthonormal (ZAMO) frame is accomplished by the Lorentz transformation $\Lambda^{\hat{\mu}}_{\mu}$, and the inverse transformation $\Lambda^{\mu}_{\hat{\mu}}$ transforms in the opposite direction. The transformation from the orthonormal basis to the comoving frame is accomplished by the boost $L^{\tilde{\mu}}_{\hat{\mu}}$ and the boost from the comoving frame to the orthonormal frame, $L^{\hat{\mu}}_{\tilde{\mu}}$. In each case, it is understood that the argument to the boost is the 4-velocity in the orthonormal frame.

Once the radiation tensor has been computed in the comoving frame (see Appendix E), it needs to be transformed to the Boyer-Lindquist frame by first boosting “down” to the orthonormal frame,

$$\mathbf{R}^{\hat{\mu}\hat{\nu}} = L^{\hat{\mu}}_{\tilde{\mu}} \mathbf{R}^{\tilde{\mu}\tilde{\nu}} \left(L^{\tilde{\nu}}_{\hat{\nu}} \right)^T \quad (22)$$

followed by the coordinate transformation to Boyer-Lindquist,

$$\mathbf{R}^{\mu\nu} = \Lambda^{\mu}_{\hat{\mu}} \mathbf{R}^{\hat{\mu}\hat{\nu}} \left(\Lambda^{\nu}_{\hat{\nu}} \right)^T \quad (23)$$

It is also possible to combine these transformations,

$$\mathbf{R}^{\mu\nu} = \left(\Lambda^{\mu}_{\hat{\mu}} L^{\hat{\mu}}_{\tilde{\mu}} \right) \mathbf{R}^{\tilde{\mu}\tilde{\nu}} \left(\Lambda^{\nu}_{\hat{\nu}} L^{\hat{\nu}}_{\tilde{\nu}} \right)^T. \quad (24)$$

The expressions for the composite boost/basis transformations are given in T07.

In order to perform the boost, it is necessary to first form the 4-velocity in the Boyer-Lindquist frame from the code variables for the transport velocity V^i and Lorentz factor, W , and then transform this 4-vector to the orthonormal frame

$$U^{\hat{\mu}} = \Lambda^{\hat{\mu}}_{\mu} U^{\mu}. \quad (25)$$

It is $U^{\hat{\mu}}$ that sets the parameters of the boost transformation.

C The Diffusion Approximation

At this intermediate stage of development of the rGRMHD code, it is possible to test the new components without having need of the numerical implementation of the radiative transfer equation (RTE). This is done by working in the first-order diffusion approximation (MM84) where the radiation tensor can be constructed directly from the local temperature and density of the fluid. The comoving frame radiation tensor is given by

$$\mathbf{R}^{\hat{\mu}\hat{\nu}} = \begin{bmatrix} a_{\text{R}} T^4 & -\frac{K_{\text{R}}}{c} \nabla T \\ -\frac{K_{\text{R}}}{c} \nabla T & \frac{1}{3} a_{\text{R}} T^4 \mathbf{I} \end{bmatrix} \quad (26)$$

where $a_{\text{R}} = 7.57 \times 10^{-15} \text{ erg cm}^{-3} \text{ K}^{-4}$ is the radiation constant and K_{R} is the radiative conductivity, given by

$$K_{\text{R}} = \frac{4}{3} c \lambda_{\text{R}} a_{\text{R}} T^3, \quad (27)$$

where $\lambda_{\text{R}} = 1/\chi_{\text{R}}$ is the Rosseland mean free path, χ_{R} the Rosseland mean opacity. For the range of densities and temperatures encountered in the simulated accreting fluid, the Rosseland mean opacity, χ_{R} , can be approximated using the results of LCS91 who provide a set analytic expressions for the mean opacity of a zero-metallicity gas for a range of values that overlap the physical scenario considered here. (See Appendix F for a more extensive discussion of the scaling of code variables to astrophysical units.)

The temperature gradient, $\nabla T \equiv T_{,\hat{i}}$, that appears in the radiative flux must be computed in the comoving frame by transforming simulation data from the Boyer-Lindquist frame. From the results of the previous appendix, the gradient of any scalar quantity in the Boyer-Lindquist frame is evaluated in the comoving frame as follows:

$$\mathcal{X}_{,\hat{\mu}} = (L^{\hat{\mu}}_{\tilde{\mu}})^T (\Lambda^{\mu}_{\tilde{\mu}})^T \mathcal{X}_{,\mu} \quad (28)$$

D Extended Diagnostics

The set of evolution diagnostics described in DHK has been augmented to monitor the radiative components. The complete dumps of the code variables that are saved at regular intervals now include all components of the radiation tensor. The shell-averaged diagnostics, $\langle \mathcal{X} \rangle(r, t)$, are defined as

$$\langle \mathcal{X} \rangle(r, t) = \frac{1}{\mathcal{A}(r)} \int \int \mathcal{X} \sqrt{-g} d\theta d\phi \quad (29)$$

where the area of a shell is $\mathcal{A}(r)$ and the bounds of integration cover the full range of the θ and ϕ grids. The rGRMHD code now includes shell-averaged values of radiative energy density, $\langle \mathcal{E} \rangle$. Fluxes through the shell are computed in a similar manner, but not normalized with the area; these diagnostics now include the radial components $\langle \mathcal{F}^r \rangle$, $\langle \mathcal{P}^{rr} \rangle$, $\langle \mathcal{P}^{r\theta} \rangle$, and $\langle \mathcal{P}^{r\phi} \rangle$.

Volume-integrated quantities are computed using

$$[\mathcal{Q}] = \int \int \int \mathcal{Q} \sqrt{-g} dr d\theta d\phi. \quad (30)$$

The volume-integrated quantities computed and saved as a function of time are the total rest mass, $[\rho U^t]$, angular momentum $[\mathbf{T}_\phi^t]$, total energy $[\mathbf{T}_t^t]$ (exclusive of radiation), and total radiative energy $[\mathbf{R}_t^t]$.

In addition, the history mechanism now optionally computes and dumps ray-traced images of simulation data by invoking a ray tracing component, as discussed in Appendix E.

E Ray Tracing

The simulations that can be envisaged with both the GRMHD and rGRMHD codes provide ever-increasing realism. In order to reconcile the results of such simulations with the growing body of high-resolution observations in various parts of the electromagnetic spectrum from earth- and space-based observatories, the production of simulated emission maps is a matter of increasing importance. To this end, a ray tracing component has been added to the rGRMHD code’s history mechanism that is capable of producing ray traced images of simulated observables as would be seen by a detector (pixel array) at a large distance from the central black hole. This is accomplished by solving the geodesic equations in the Kerr metric for each pixel in this array; the manner in which this is done largely follows Reynolds *et al.* (1999), but the rGRMHD code uses analytic expressions for the turning points of the ODE describing the polar coordinate of the polar angle Θ . These solutions are solved once and coded as Chebyshev polynomials, which allows for efficient archiving and fast computation (see Press *et al.*, 1992, for the approach, though the rGRMHD code implements the compression and retrieval routines differently). Four Chebyshev polynomials are stored for each pixel, one for each Boyer-Linquist component of a photon trajectory; i.e. $T(\lambda)$, $R(\lambda)$, $\Theta(\lambda)$, and $\Phi(\lambda)$, where λ is an affine parameter common to all four polynomials for each geodesic. The polynomials are interrogated through this common parameter as part of the history calculations to map a particular emission event in the simulation data to a particular pixel in the image plane. Photons emitted from different regions of the simulation volume do not arrive at the pixel plane at the same time, so the code maintains a stack of pixel planes, and maps arrival times to a particular pixel array in this stack. When a given pixel array in the stack slips out of causal contact with the simulation data it is flushed to memory as a completed image. The array in question is cleared and placed at the far end of the pixel stack to receive data from the portions of the simulation volume just coming into causal contact with the pixel stack. This ring buffer structure keeps memory usage to a minimum. The pixel stacks produced by this tool allow the production of static (time-averaged or instantaneous) and animated emission maps.

Ray tracing stops at unit optical depth. Currently, no attempt is made to account for refraction or reflection of photons on their flight to the pixel plane.

Several types of emission map can be constructed by the ray tracer, depending on the needs of a particular simulation. Since the full range of code variables can be accessed by the history mechanism, the range of possible maps that can be produced is quite broad. For the simulations described in this paper, ray tracing was not used. In part, this is due to the fact that axisymmetric simulations are not conducive to ‘realistic’ ray tracing, even though the ray tracer does render images by wrapping observables around the full azimuth. To better see the capabilities of the ray tracer, Figure 6 shows a test image from an unpublished 3D simulation analogous to model KDP

of DHK (main difference, $\Gamma = 4/3$ instead of $5/3$). The fully ray traced image is a projection of Poynting flux, onto the geodesic's tangent vector, $\mathbf{T}^t_{\mu(EM)} \mathcal{X}^\mu$. Though various emission maps have been tested, the Poynting flux maps remain the most appealing for simple demonstrations in that they capture in a single image the cool disk, the hot plunging flow near the black hole, and the wispy traces of the funnel outflow and jet. Ray traced images from axisymmetric simulations are far less appealing due to pervasive artifacts due to the axisymmetric grid, and are not reproduced here.

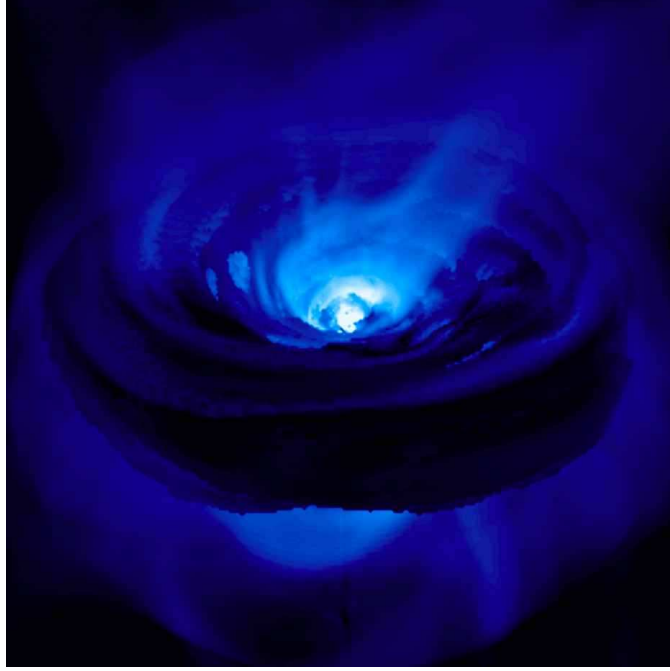


Figure 6: Ray Traced Image of Poynting Flux in 3D GRMHD Simulation

The rGRMHD code is an MPI-based parallel application that uses a form of domain decomposition to achieve good performance on parallel platforms. Introducing ray tracing in this context could adversely affect performance because the process of tracing photons through the simulation volume could introduce severe performance bottlenecks. To maintain performance, a client-server model was adopted where many ray tracing functions are handled by a processor dedicated to this task, freeing the remaining processors to carry out the task of evolving the simulation. Some computational burden remains with the simulation processors as part of the existing history mechanism, but this burden is well balanced and does not degrade parallel performance (i.e. scalability), though it does add considerably to the turn-around time for a simulation so that ray tracing remains a very expensive optional feature for simulations.

F Calibration and Unit Conversion

The rGRMHD code uses relativistic units ($G = c = 1$), with a central black hole taken to have unit mass ($M_{bh} = 1$). The opacity functions that are used during the construction of the radiation tensor are expressed in cgs units, and are functions of the density and temperature of the gas, which are evaluated in code units; to express the radiation tensor in code units, it is therefore necessary to scale the code units to physical units (cgs), and vice-versa. Furthermore, the test fluid approximation which is used in the GRMHD numerical scheme effectively decouples the mass of the accreting fluid from that of the central black hole, so that the initial state can be assigned an arbitrary density, along with an internal energy that is scaled in relation to this density to distinguish between “hot” and “cold” initial tori. However, when a radiative component is introduced, this arbitrary scaling is no longer appropriate since radiative effects must be tied to the mass/energy and time scales of the central black hole. Therefore, both the initial state and the evolving fluid variables must be calibrated to an astrophysical scenario to correctly capture radiative effects.

The initial state consists of a torus with an inner edge at $r_{in} = 6.8 M_{bh}$, an outer edge at $r_{out} \approx 30 M_{bh}$ and a scale height of $h \approx 6.1 M_{bh}$, measured on the $0.01 \epsilon_{max}$ contour at the pressure maximum. In order to match this initial state to an astrophysical scenario, assume that the torus contains 100 solar masses of gas at a temperature of ~ 100 K, and that it orbits a supermassive black hole 10^8 solar masses.

For this choice of parameters, we derive a mean physical density $\bar{\rho}_{(cgs)}$ which can be compared during initialization to the grid-averaged density in code units. The density scaling parameter is set accordingly as

$$\eta = \frac{\bar{\rho}_{(cgs)}}{\bar{\rho}_{(code)}} \quad (31)$$

and is subsequently used to convert the density variable during simulations.

The temperature scaling parameter

$$\xi = \frac{T_{(cgs)}}{T_{(code)}} \quad (32)$$

converts between the two sets of units during the simulation, where $T_{code} \equiv (\Gamma - 1) \epsilon = (\Gamma - 1) E/D$. This parameter is also set from the initial conditions by computing the ratio of the mean physical temperature (a model-dependent parameter) and the grid-averaged temperature in code units of the initial torus.

The scaling parameters η and ξ are used to convert density and temperature during the computation of the Rosseland mean opacity, $\chi_{R(cgs)}$, using the approximation supplied by LCS91. Once $\chi_{R(cgs)}$ has been calculated, it is converted to code units and used to construct the radiation tensor in the comoving frame.

To construct $\mathbf{R}^{\mu\nu}$, we need to express the radiation constant, a_R , and the radiative conductivity, K_R , in code units. The radiation constant can be set during initialization by relating initial values of the dimensionless ratio of the time-time components of the fluid energy momentum tensor and

the radiation tensor,

$$\frac{\mathbf{T}_{(\text{fluid})}^{tt}}{\mathbf{R}^{tt}} \quad (33)$$

which must remain unchanged in converting from cgs to code units. In general,

$$\mathbf{T}_{(\text{fluid})}^{tt} = \rho h (U^t)^2 + g^{tt} P = -\frac{g^{tt}}{W} [(D + \Gamma E) W^2 - (\Gamma - 1) E] \quad (34)$$

This expression can be simplified considerably, however, since $\mathbf{T}_{(\text{fluid})}^{tt}$ is to be evaluated for the initial torus, for which $W \approx 1$, and $g^{tt} \approx -1$ in the vicinity of the disk pressure maximum. To a very good approximation, $\mathbf{T}_{(\text{fluid})}^{tt}$ can be approximated by the rest-energy of the initial torus, so $\mathbf{T}_{(\text{fluid})(\text{code})}^{tt} \approx \rho_{(\text{code})}$ and $\mathbf{T}_{(\text{fluid})(\text{cgs})}^{tt} \approx \rho_{(\text{cgs})} c^2$. With the rest energy scaling parameter

$$\zeta = \frac{\rho_{(\text{cgs})} c^2}{\rho_{(\text{code})}} = \eta c^2 \quad (35)$$

it follows that the dimensionless ratio can be approximated as follows:

$$\frac{\mathbf{T}_{(\text{fluid})}^{tt}}{\mathbf{R}^{tt}} \rightarrow \frac{\rho_{(\text{code})}}{a_{\text{R}(\text{code})} T_{(\text{code})}^4} = \frac{\rho_{(\text{cgs})} c^2}{a_{\text{R}(\text{cgs})} T_{(\text{cgs})}^4}, \quad (36)$$

and the radiation constant $a_{\text{R}(\text{code})}$ can be obtained

$$a_{\text{R}(\text{code})} = a_{\text{R}(\text{cgs})} \frac{\xi^4}{\zeta} \quad (37)$$

The radiative conductivity is given by (MM84)

$$K_{\text{R}} = \frac{4}{3} c \lambda_{\text{R}} a_{\text{R}} T^3, \quad (38)$$

where $\lambda_{\text{R}} = 1/\chi_{\text{R}}$ is the Rosseland mean free path. The Rosseland mean free path (units cm^{-1}) is converted to code units by using the length-scale conversion

$$r_{\text{g}(\text{code})} = 1 \rightarrow r_{\text{g}(\text{cgs})} = \frac{G_{(\text{cgs})} M_{\text{bh}(\text{cgs})}}{c_{(\text{cgs})}^2} \quad (39)$$

G Initial State - Torus with Thermal Radiation

This Appendix reviews the initialization used in the earlier DHK03 simulations and discusses how the initial state needs to be modified to study radiative effects.

G.1 Initial Torus - Fluid Variables

The initial state consists of a thick torus with a nearly-Keplerian distribution of angular momentum, with specific angular momentum given by $l = -U_\phi/U_t$ and angular velocity $\Omega = U^\phi/U^t$. DHK03 provides a detailed derivation of the following analytic expression for the internal energy of the disk,

$$\epsilon(r, \theta) = \frac{1}{\Gamma} \left(\frac{U_{in} f(l_{in})}{U_t(r, \theta) f(l(r, \theta))} - 1 \right). \quad (40)$$

where U_t represents the binding energy, U_{in} the surface binding energy, and $f(l) = \|1 - k l^{\alpha+1}\|^{1/(\alpha+1)}$. The parameter α is related to the disk structural parameter q by $\alpha = q/(q-2)$. Also, $k = \eta^{-2/(q-2)}$ and η is a constant used in constructing the power-law rotation for the initial torus,

$$\Omega = \eta \lambda^{-q} \quad (41)$$

where λ is given by

$$\lambda^2 = \frac{l}{\Omega} = l \frac{(g^{tt} - l g^{t\phi})}{(g^{t\phi} - l g^{\phi\phi})}. \quad (42)$$

For a constant entropy adiabatic gas the pressure is given by $P = \rho \epsilon (\Gamma - 1) = K \rho^\Gamma$, and density is given by $\rho = [\epsilon (\Gamma - 1)/K]^{1/(\Gamma-1)}$.

A particular disk solution is specified by choosing the parameter q , the entropy parameter K , and the angular momentum l_{in} at r_{in} , the inner edge of the disk. For all simulations, the location of the inner edge, $r_{in} = 6.80 M_{bh}$, as well as parameters $K = 0.01$, $q = 1.66$, and $l_{in} = 3.34$ are kept fixed.

G.2 Initial Torus - Magnetic Field

The initial magnetic field is obtained from the definition of $F_{\mu\nu}$ in terms of the 4-vector potential, A_μ , $F_{\mu\nu} = \partial_\mu A_\nu - \partial_\nu A_\mu$. Our initial field consists of axisymmetric poloidal field loops, laid down along isodensity surfaces within the torus by defining $A_\mu = (A_t, 0, 0, A_\phi)$, where

$$A_\phi = \begin{cases} k(\rho - \rho_{cut}) & \text{for } \rho \geq \rho_{cut} \\ 0 & \text{for } \rho < \rho_{cut} \end{cases}, \quad (43)$$

where ρ_{cut} is a cutoff density corresponding to a particular isodensity surface within the torus. Using the above definition, it follows that $\mathcal{B}^r = -\partial_\theta A_\phi$ and $\mathcal{B}^\theta = \partial_r A_\phi$. The constant k is set by the input parameter β , the ratio of the gas pressure to the magnetic pressure, using the volume-integrated gas pressure divided by the volume-integrated magnetic energy density in the initial

torus. We use $\beta = 100$ in all runs. The constant ρ_{cut} is chosen to keep the initial magnetic field away from the outer edge of the disk. Here we use $\rho_{cut} = 0.5\rho_{max}$, where ρ_{max} is the maximum density at the center of the torus, to ensure that the initial field loops are confined well inside the torus.

G.3 Initial Torus - External Medium

The region outside the torus is initialized to a numerical vacuum that consists of a cold, tenuous, non-rotating, unmagnetized gas. The auxiliary density variable, D , in the vacuum is set to seven orders of magnitude below the maximum value of D in the initial torus. Similarly, the auxiliary energy variable E is set ten orders of magnitude below the initial maximum of E . These values define the numerical floor of the code, below which D and E are not allowed to drop. In practice, the numerical floor is rarely asserted during a simulation, since outflow from the evolving torus quickly populates the grid with a gas that, though of low density, lies above the numerical floor. Further details on the numerical floor are given in DH03.

G.4 Initial Torus - Radiation Tensor

Once the hydrodynamic variables have been initialized, the radiation tensor in the diffusion approximation is set using the temperature and density distributions. The radiation tensor is computed from the initial state using the same routines that compute its values during the simulation. The following procedure is carried out in each computational zone:

1. density and temperature converted to cgs units (Appendix F)
2. Rosseland mean opacity computed from these values (Appendix C)
3. Rosseland mean converted to code units (Appendix F)
4. comoving-frame radiation tensor computed from temperature and opacity (Appendix C), and also from temperature gradient in comoving frame (Appendix B)
5. comoving-frame radiation tensor converted to Boyer-Lindquist frame (Appendix B)